

Growth, optical, luminescence, thermal, mechanical and etching studies of a Mixed Alkali Oxalate $K_{0.56}(NH_4)_{0.44}(H_2C_2O_4)(HC_2O_4)(H_2O)_2$ single crystal

M. NIROSHA, S. KALAINATHAN*

Center for Crystal Growth, VIT University, Vellore – 632014, Tamilnadu, India

Single crystals of mixed alkali oxalate $K_{0.56}(NH_4)_{0.44}(H_2C_2O_4)(HC_2O_4)(H_2O)_2$ have synthesized and grown by slow evaporation solution growth technique. The structural, thermal, optical and mechanical property has studied for the grown crystal. Single crystal xrd revealed that the crystal belongs to triclinic system with space group P-1. The presences of functional groups in the crystallized material have confirmed using the FTIR vibrational spectrum. The optical absorbance spectrum from 190 to 1100 nm shows the cut-off wavelength occurs at 300 nm. The material shows its transparency in the entire region of the visible spectrum. The PL spectrum of the title compound shows the peak observed at 520 nm is due to the ligands present in the compound. Thermogravimetric and differential thermal analysis reveal the thermal stability of the grown crystal. Etching study reveals the surface features of the grown crystal. The Vickers microhardness studies have carried out on the (100) plane to understand the mechanical properties of the grown crystal. Mechanical hardness of the grown crystal MAO has studied, and Vickers hardness number has calculated. The hardness of the title compound increases on increasing the load. The Meyer's index number (n), and the stiffness constants for different loads has calculated and reported.

(Received September 10, 2013; accepted January 22, 2014)

Keywords: Crystal growth, Thermogravimetric analysis, Luminescence, Mechanical studies, Etching studies

1. Introduction

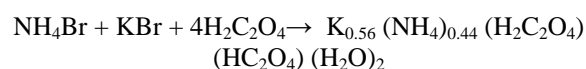
There is almost no limit to the combination of inorganic and organic components in the formation of hybrid materials [1]. During the past decades, the ongoing synthesis and exploitation for novel organic-inorganic hybrids are of remarkable interest because of their meaningful architectures and potential applications recommend them as candidates for adsorption materials, luminescent sensors and magnetic materials [2]. A hybrid material gives rise to intriguing phenomena and new functionality that may not be achievable by either inorganic or organic constituents alone. The potential applications of hybrid materials lie in their use as sorbents, catalysis, gas separation and charge storage materials [3]. The important application in the area of crystalline hybrid materials is the possibility to create multifunctional material from single complexes to multi- dimensional coordination polymers. They allow the design of new architectures with various topologies and gives rise to three-dimensional connectivity [4]. In recent decades, metal ions associated with organic ligands have generated a group of privileged hybrids. The oxalate anion is a particularly versatile ligand that can adopt many kinds of coordination modes. As simplest dicarboxylate unit, the oxalate anions adopt various coordination modes such as monodentate, bidentate, and combinations of both mono- and bidentate to facilitate the formation of extended structures. It is a good bridging ligand, coordinating to metal ions for preparation of inorganic frameworks [5]. In

this rapid growing field, some researchers focused on the synthetic manipulation of crystalline organic-inorganic hybrid materials. Up to now there is no report concerning the physical properties of the above compound, which are most important for the material to be used in applications.

2. Experiment

2.1 Material synthesis

The commercially available ammonium bromide, potassium bromide and oxalic acid have used for the synthesis. The starting materials have taken in 1:1:4 stoichiometric ratios and dissolved in an aqueous solution. The homogeneous temperature with uniform concentration has obtained using an immersible Stirrer. This solution evaporated to dryness for 3 hrs gives rectangular shape crystals. The synthesized material was further purified by repeated recrystallization process. The title compound has synthesized based on the following reaction scheme:



Unit cell contains two cationic sites occupied randomly by K^+ and NH_4 , four oxalate groups and four water molecules. Charge balance in the reaction has maintained by one monoanion $HC_2O_4^-$ and one fully protonated diacid $H_2C_2O_4$ for every cationic site [4].

2.2 Solubility

The solubility of MAO has determined in the temperature range 30-45°C. This process has repeated for every 5°C using an ultra cryostat with accuracy of $0.01 \pm ^\circ\text{C}$. The solubility for 30°C has determined by dissolving MAO salt in 100ml of water taken in an air tight container maintained at the temperature with continuous stirring of the solution. In the saturated solution, 5ml has pipetted out and then poured into a Petri dish of known weight. The amount of the salt present in 5ml of the solution has measured by subtracting the empty beaker's weight. From this, amount of the salt present in 100ml of the solution have found out. In the same way, the amount of salt dissolved in 100ml at 35, 40, 45°C has determined. Fig.1 shows the solubility curve of MAO salt.

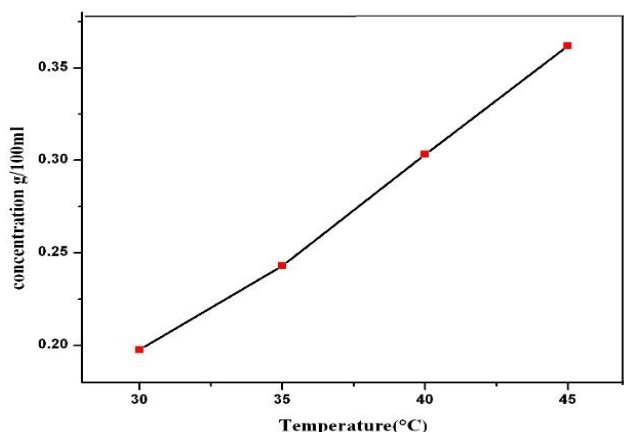


Fig. 1. Solubility of MAO.

2.3 Crystal growth

The single crystals of MAO have grown using slow evaporation technique at ambient temperature. The Purified MAO salt has used for growing bulk single crystals. A saturated solution has prepared at room temperature by using water as a solvent. The temperature of the solution has risen by 5°C above the room temperature in order to obtain a homogeneous solution of MAO in water. The filtered solution has risen by 3°C above the room temperature. The defect free seed crystal has introduced into the mother solution. The beaker containing the saturated solution has optimally covered for controlled evaporation of the solvent. A transparent single crystal of size 5 mm × 4 mm × 2 mm have obtained in a period of 10 days. The photographs of the as grown MAO crystal have shown in Fig. 2 respectively.



Fig. 2. Grown crystals of MAO.

3. Results and discussion

3.1 Single crystal xrd

The single crystal X-ray diffraction data have collected using ENRAF NONIUS CAD4 X-ray diffractometer with MoK_α radiation with the wavelength of 0.71073 \AA . The calculated cell parameters are $a = 6.34 \text{ \AA}$, $b = 7.04 \text{ \AA}$, $c = 10.56 \text{ \AA}$, $\alpha = 93.96^\circ$, $\beta = 101.19^\circ$, $\gamma = 99.74^\circ$ and $V = 453 \text{ \AA}^3$ and it belongs to triclinic system with space group P-1. The unit cell parameters and space group are in good agreement with the reported values [4]. Thus confirms the grown crystal. The crystal morphology is a field of vital interest to various applications as many crystal physical properties are implicitly dependent on their shapes. Fig. 3 shows the morphology diagram of the grown crystal.

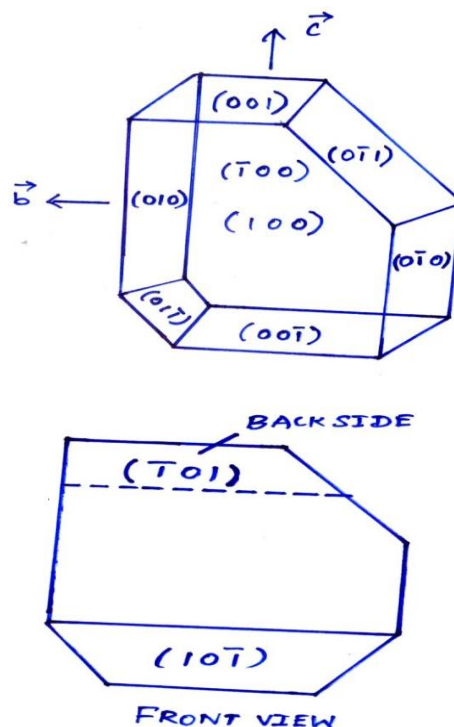


Fig. 3. Morphology diagram of MAO.

3.2 FT-IR spectral studies

FT-IR spectrum helps to identify the functional groups and molecular structure of the synthesized compound [6]. FTIR spectral analysis of the grown crystal has recorded in the range 400-4000 cm^{-1} . It has carried out using FT-IR 4100 type-A spectrophotometer employing KBr pellet technique at room temperature. Fig.4 shows the recorded spectrum of the MAO crystal. The infrared spectrum shows an intense band at 3427 cm^{-1} is due to ν (O-H) vibration. The peak observed at 3296 cm^{-1} is due to the ν (N-H) bending mode of vibration. The band observed at 1691 cm^{-1} is due to asymmetric vibration of CO_2^- groups. The vibration observed at 1402 cm^{-1} is due to the symmetric vibration of CO_2^- groups. The peak observed at 1120 cm^{-1} is due to O-C=O vibrations. The peak observed in the low frequency region of 478.35 cm^{-1} , and 721.38 cm^{-1} is due to the presence of O-C=O in and out of plane bending vibrations. The comparison of IR bands with

$\text{Rb}_{0.86}(\text{NH}_4)_{0.14}(\text{H}_2\text{C}_2\text{O}_4)(\text{HC}_2\text{O}_4)(\text{H}_2\text{O})_2$ [4] as a function of temperature in the range 320-460K as shown in Table 1.

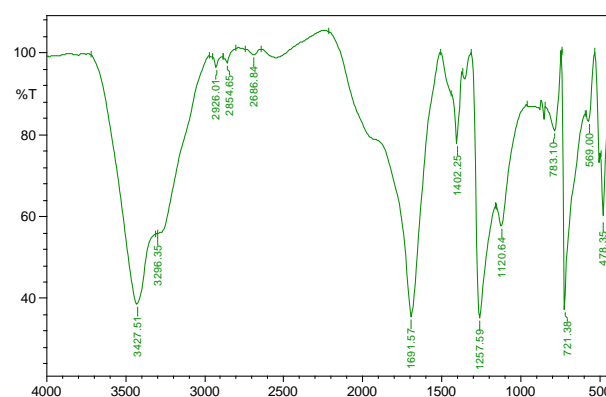


Fig. 4. FTIR spectrum of MAO.

Table 1. Band assignment for FTIR spectrum of MAO.

Assignments	obtained values At room temperature	$\text{Rb}_{0.86}(\text{NH}_4)_{0.14}(\text{H}_2\text{C}_2\text{O}_4)(\text{HC}_2\text{O}_4)(\text{H}_2\text{O})_2$ at 320-469K
ν (O-H) vibration	3427	4000-3000
ν (N-H) bending	3296	-
CO_2^- asymmetric vibration	1691	1637-1880
CO_2^- symmetric vibration	1402	1403-1400
C=O stretching vibration	1120.64	1249-1027
O-C=O in plane bending	721	720
O-C=O out of plane bending	478	475

3.3 UV-vis spectrum analysis

The UV-vis spectrum has recorded for the grown MAO crystal using ELICO SL 218 double beam UV-vis spectrophotometer in the range 190-1100 nm. The absorbance spectrum occurs due to the electronic transitions of the molecule. Fig.5 shows the absorption spectrum of the MAO crystal (2mm thick). From the spectrum, it reveals that the UV lower cutoff wavelength

occurs at about 300 nm. The absence of absorption in the entire visible region of the spectrum shows it could be used for optical window applications [7]. The highest peak observed at 229 nm is due to the $n-\pi^*$ transition. The absorption coefficient (α) can be expressed by the formula

$$\alpha = \frac{2.3026 \log(1/T)}{t} \quad (1)$$

Where T is the transmittance and t is the thickness of the crystal.

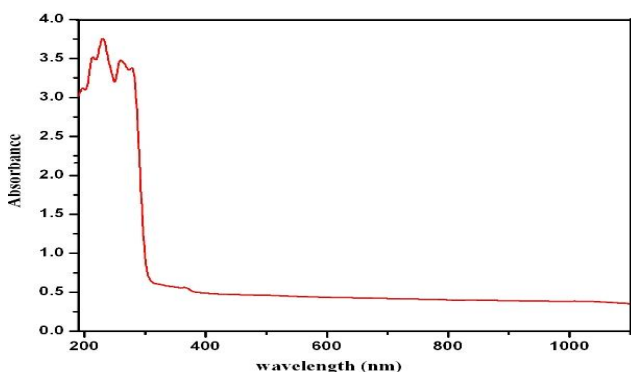


Fig. 5. Uv-vis absorbance spectrum of MAO.

The relation between the optical band gap, absorption coefficient and energy ($h\nu$) of the incident photon has given by

$$\alpha h\nu = B(h\nu - E_g)^{1/2} \quad (2)$$

Where E_g the optical energy gap, B is a constant, h is Planck's constant and ν the incident photons. Optical band gap value has calculated by plotting between the absorption coefficient $(\alpha h\nu)^{1/2}$ and photon energy ($h\nu$). The band gap obtained from the graph for MAO has shown in Fig. 6. The optical band gap value of MAO is 4.05 eV. The wide band gap of the title material shows that it may possess high damage threshold and large transmittance in the visible region [8-9]. Wide band gap material will enable higher voltage equipment, a crucial requirement for the electric warship [10].

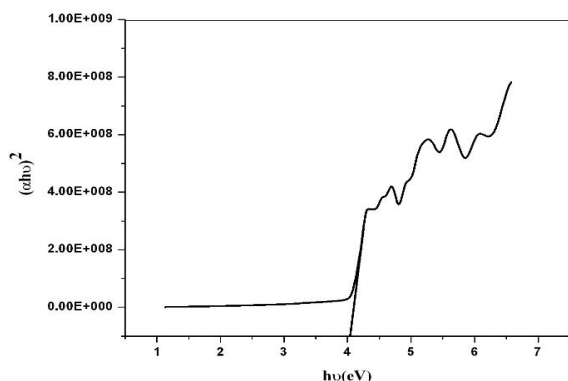


Fig. 6. plot of $h\nu$ vs. $(\alpha h\nu)^{1/2}$

The extinction coefficient is a measure of the fraction of light lost due to scattering and absorption per unit distance of the penetration medium. It can be estimated from the values α and λ using the relation

$$K = \frac{\lambda \alpha}{4\pi} \quad (3)$$

The extinction coefficient as a function of photon energy has shown in Fig. 7. The extinction coefficient decreases with energy shows that light lost during the scattering and absorbance decreases.

$$n = \frac{-(R+1) \pm 2\sqrt{R}}{(R-1)} \quad (4)$$

The wavelength dependent refractive index for MAO crystal has shown in Fig. 8. The refractive index increases with increasing wavelength. The refractive index (n) is 1.72 at 1100nm for MAO crystal.

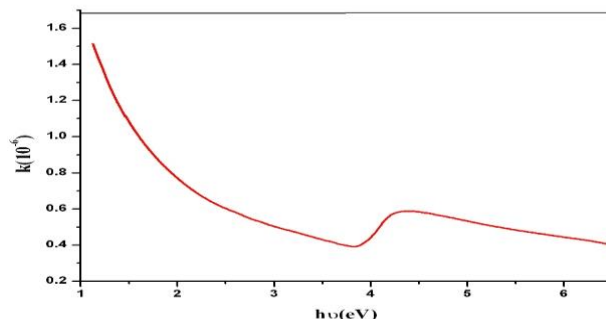


Fig. 7. plot of $h\nu$ vs. k .

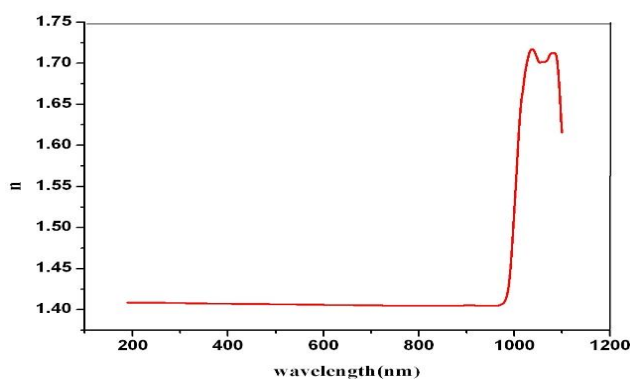


Fig. 8. plot of wavelength vs. refractive index.

3.4 TG/DTA studies

Differential thermal analysis (DTA) and Thermo gravimetric analysis (TGA) give information regarding the phase transition and decomposition stages of the crystal system [11]. The thermal analyses have carried out using a SDT Q600 V8 apparatus at a heating rate of $10^\circ\text{C}/\text{min}$ in the temperature range 30°C to 1000°C at nitrogen atmosphere. The characteristic curve of TGA and DTA of the compound has shown in Fig. 9 (a&b). TGA curve precisely shows the three stages of weight losses occur at 93.13°C , 180°C , and 548°C . During heating, MAO decomposes, releasing the oxalate ions, NH_4 , CO and the release of crystalline water. The DTA Thermo gram

reveals three exothermic peaks at 112°C, 195°C and 235°C. The peak observed at 112°C can be attributed to a structural phase orientation probably due to the reorientation of ammonium tetrahedral [12]. The second peak at 195°C can be attributed to the ferroelectric-paraelectric phase transition. The third peak observed at 235°C represents the decomposition point of the material due to super-protonic phase transition linked with the breaking of two types of hydrogen bond (O-H...O) and (N-H...O) [12-15].

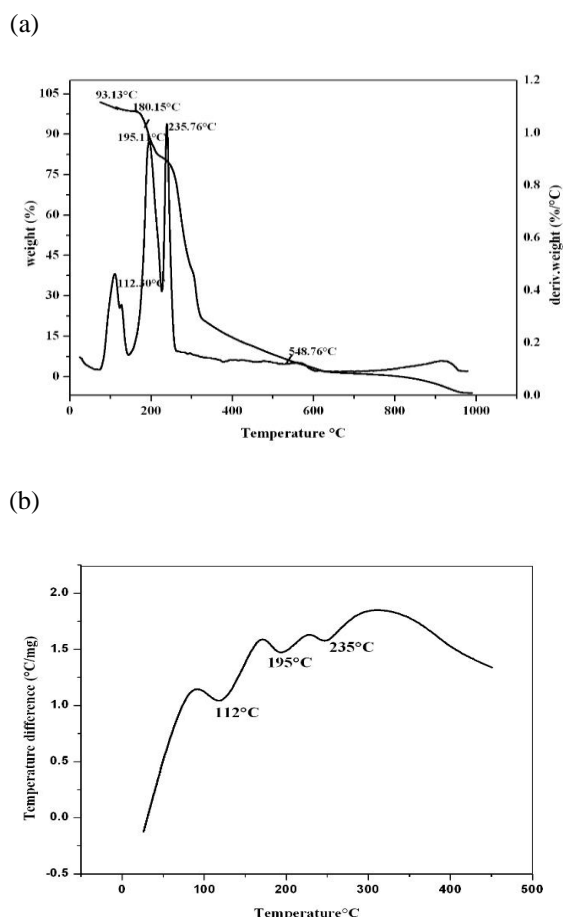


Fig. 9 (a&b).TG/DTA spectrum of MAO.

3.5 Photoluminescence study

The PL spectrum have recorded using JobinYvon-Spexspectrofluorometer (Fluorolog version 3: Model FL3-11) at room temperature; 450W high pressure xenon lamp acts as an excitation source. The recorded emission spectrum has shown in Fig.10. The maximum intensity observed at 520 nm is due to the ligand based luminescence. When there is no electronic interaction occurs, between the organic and inorganic moieties, leading to ligand-based luminescence [16]. This is due to electronic configuration of metal and the degree of orbital overlap between the organic and inorganic moieties.

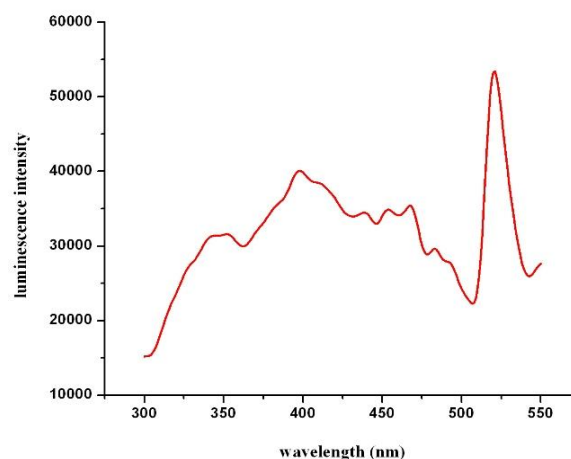


Fig. 10. Photoluminescence spectrum of MAO.

3.6 Etching

Chemical etching is a very simple and elegant technique to reveal the crystal defects and the crystal growth mechanism. Etching technique helps to develop some features such as growth striations, etch spirals; rectangular etch pits etc., on the crystal surface. The various types of etch pits have observed at room temperature for varying times. An etching on the surface has carried out by dipping the crystal and wiping with dry filter paper. For etching purpose, thin crystal of 3 mm thickness has cut from the grown crystal. Etching studies has performed on as-grown (100) face. Surface layer has removed by means of etching a fresh surface appeared gave clear etch pits. Etch patterns have analyzed using a Carl Zeiss metallurgical microscope (Axios kop 40 MAT) in the reflection mode. Fig. 11(a) shows the photomicrograph of the grown crystal before etching. When etched with water for 30s, there is no observation of etch pits and as shown in Fig. 11(b). When the etching time increased for 45s, small rectangular growth hillocks have observed which as shown in Fig. 11(c). The directions of the dislocation lines have revealed by the shape of the etch pits. As etching time increases for 60s, the rectangular hillock got elongated in their size but the pit pattern remains same which as shown in Fig. 11(d). The observed etch pits are due to the presence of dislocation caused by thermal stresses which is imposed on the growth surface [17].

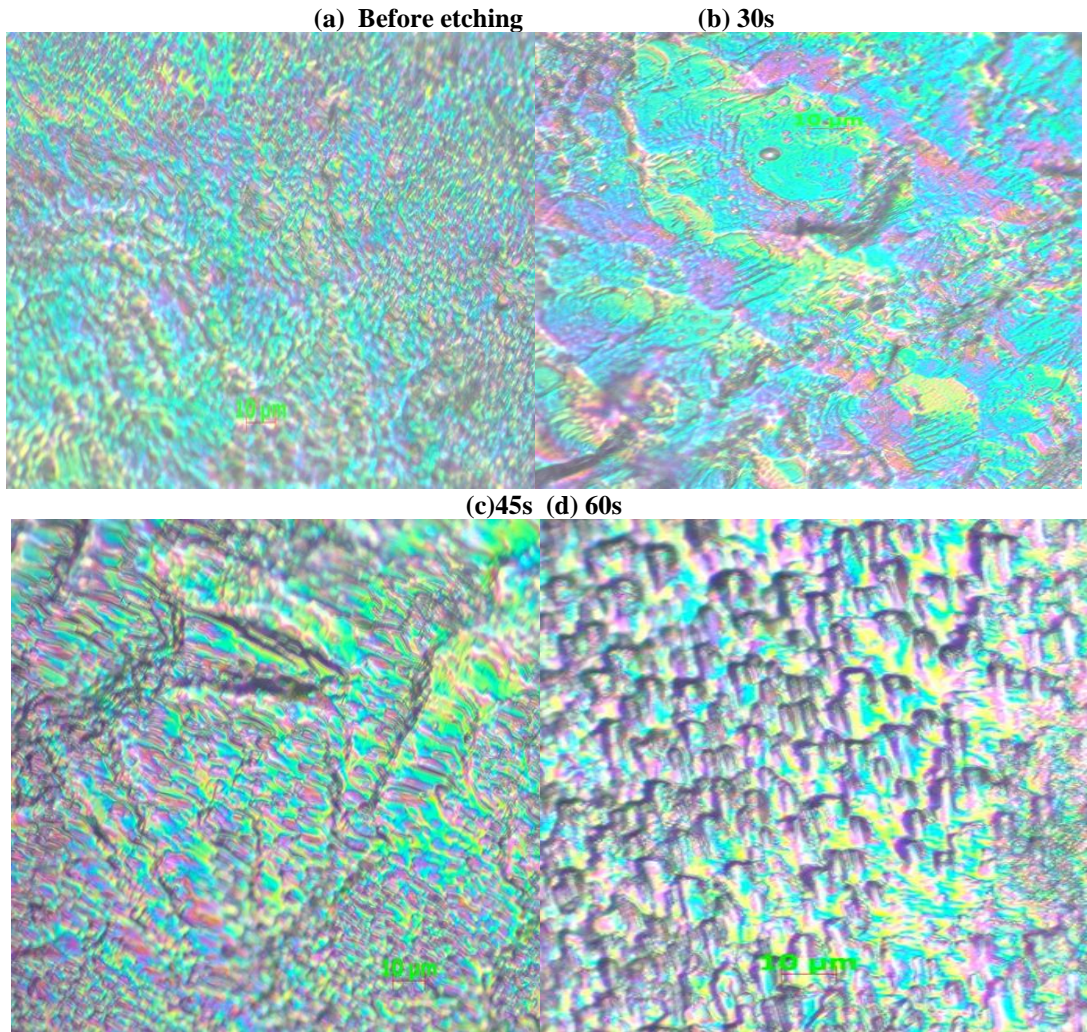


Fig. 11. Etching pattern of grown crystal with different periods (a) before etching (b) 30s (c) 45s (d) 60s.

3.7 Micro hardness studies

The hardness of the material plays a major role in device fabrication. The Hardness of the crystal carries information about the crystal structure of the material. Micro hardness studies have applied to understand with plasticity of the substance [18]. Experiment has carried out with Mututoyo MH-112 micro hardness tester using Vickers diamond pyramidal indenter attached to a metallurgical microscope. Crystal with flat and smooth faces free from any defects has chosen for the static indentation tests. The indentations have made at room temperature with a constant indentation time of 10s. Vickers microhardness test has carried out on (100) face of the grown crystal. The surface has gently polished with water. Then the polished crystal has properly mounted on the base of the microscope and indented gently by applying loads 10-100g with a dwell time of 10s. At least five indentations have made on sample for each load. The indented surface has examined under the microscope. The lengths of the two diagonals of the indentations have measured by a calibrated micrometer attached to the eyepiece of the microscope after unloading. The average

diagonal lengths measured at each time. The Vickers microhardness number of the crystal H_v has calculated using the formula.

$$H_v = 1.8544 \frac{P}{d^2} \quad (5)$$

Where P is the load applied, and d is the mean diagonal length of the indentation. Fig.12 shows the plot between load (P) and (H_v) of MAO single crystal. It is evident from the plot that the microhardness value increases with the load shows the reverse indentation size effect [19]. The Meyers index number has calculated from Meyer's law which gives the relation between the load and indentation diagonal length.

$$P = kd^n \quad (6)$$

$$\log p = \log k + n \log d \quad (7)$$

Where k is the material constant and n, is the Meyer's index. The plot of $\log p$ against $\log d$ is a straight line, and it as shown in Fig. 13. The slope of the graph gives n, and

it has found to be 2.33 respectively. Vickers hardness value should increase with the increase of P if $n > 2$ and decrease in $n < 2$. The calculated 'n' value agrees well with the experimental values. According to Onitsch and Hanneman, n should lie between 1 and 1.6 for harder materials and above 1.6 for softer materials [20]. Thus, MAO crystal belongs to soft material category.

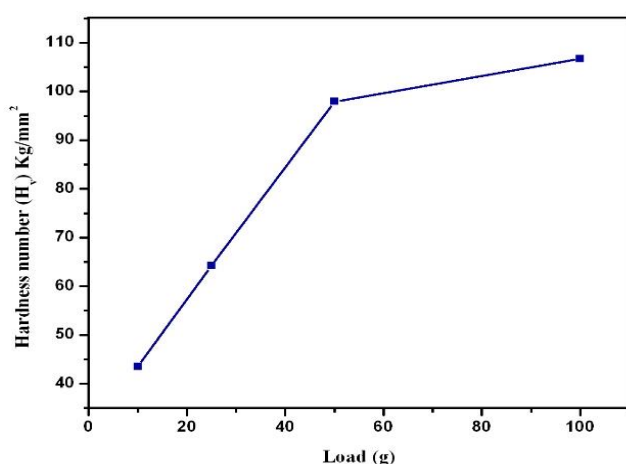


Fig. 12. Load vs. Hardness number (Hv).

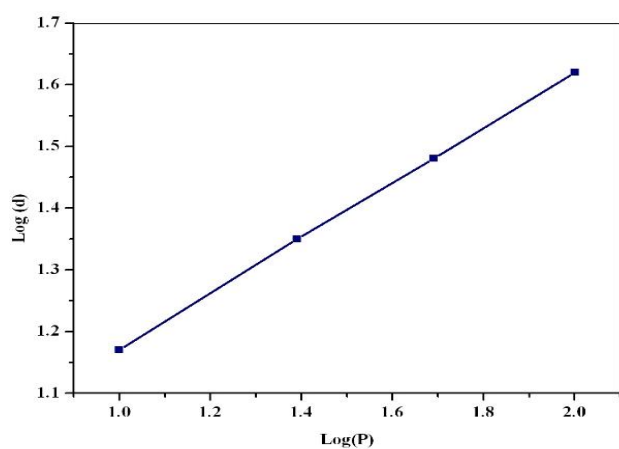


Fig. 13. log p vs. log d.

The elastic stiffness constant (C_{11}) for different loads calculated using Wooster's empirical formula $C_{11} = H_v^{7/4}$ [21]. It gives an idea about the tightness of bonding between neighboring atoms [22]. Fig.14 shows the stiffness constant with load, stiffness constant increases with increasing load.

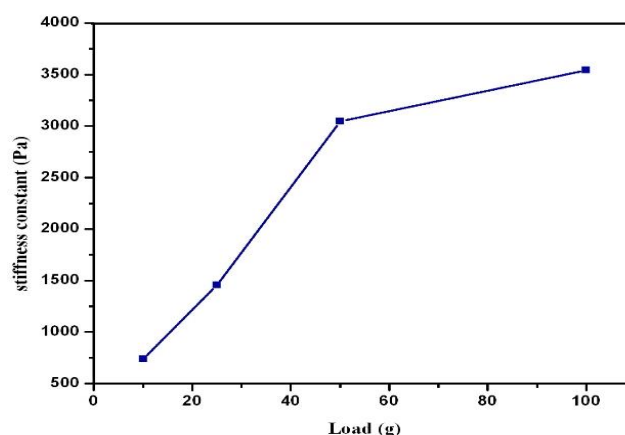


Fig. 14. Load vs. stiffness constant.

4. Conclusions

Good quality single crystals of MAO have grown by the slow evaporation solution growth technique. Single crystal xrd revealed the lattice parameters and space group. The presences of functional groups have identified using FTIR spectrum. The UV-vis spectrum shows that the MAO crystals are highly transparent in the visible region, and the optical band gap of the material has calculated. The thermal stability of the crystal have identified using TG/DTA spectrum. The photoluminescence analysis shows the maximum intensity observed at 528 nm is due to the presence of ligand in the compound. The etching study reveals the dislocations present in the crystal. The Vickers hardness number of the grown crystal increases with increasing load due to the reverse indentation size effect. The calculated value of Meyer's index n of the grown crystal is greater than 1.6 and reveals its soft nature.

Acknowledgements

The author acknowledges Dr. U. Madhusoodanan, IGCAR for PL studies and SAIF, IIT madras for proving the S-XRD facility. The authors are also thankful to VIT University for providing excellent research facilities.

References

- [1] Guido Kickelbick, Hybrid Materials: Synthesis, characterization and applications, 1st ed., John Wiley & Sons, Weinheim, 2007.
- [2] Y. Liu, Q. Wang, L. Chen, H. Zhao, J. Zhao, Syn. Metals, **162**, 1648 (2012).
- [3] Elisabeth Irran, Thomas Bein, and Norbert Stock, J. Solid State Chem, **173**, 293 (2003).
- [4] M. Hamdouni, L. Agengui, S. Walha, A. Kabadou, A. B. Salah, J ChemCrystallogr **41**, 1742 (2011).
- [5] X. Xiao, Y. Wei, W. Zheng, K. Wu. Z. Anorg. Allg. Chem, **637**,741(2011).
- [6] A. Philominal, S. Dhanuskodi, J.Philip, Mater. Chem. Phys, **139**, 1 (2013).

- [7] Li Li, Z. Wang, X. Song, S. Sun, *SpectrochimActa part A*, **72**, 1816 (2009).
- [8] A. Ashour, N. El-Kadey, S.A. Mahmoud, *Thin solid films*, **269**, 117 (1995).
- [9] C. T. Chen, L. Bai, Z. Z. Wang, R. K. Li, *J. Cryst. Growth*, **292**,169 (2006).
- [10] T. Ericson, *Proc. IEE* **6**, 1077 (2002).
- [11] S. Gunasekaran, G. Anand, R. ArunBalaji, J. Dhanalakshmi, S. Kumaresan, *Pramana - J. Phys.*, **75**, 683 (2010).
- [12] M. Abdelhedi, L. Ktari, M. Dammak, A. Cousson, A. W. Kolsi. *J Alloys Compd*, **460**,147 (2008).
- [13] L. Ktari, M. Dammak, T. Mhiri, A.W. Kolsi. *Phys. Chem. News* **8**, 01 (2008).
- [14] M. Djemel, M. Abdelhedi, L. Ktari, M. Dammak. *J. Mol. Struct.* **1047**, 15 (2013).
- [15] M. Djemel, M. Abdelhedi, M. Dammak, A.W. Kolsi. *J. Mol. Struct.* **1033**, 84 (2013).
- [16] David Farrusseng, *Metal-organic Frameworks: Applications from catalysis to Gas storage*, 1sted, John Wiley & Sons, Weinheim, 2011.
- [17] G. Ravi, K. Srinivasan, S. Anbukumar, P. Ramasamy, *J. Cryst. Growth* **137**, 598 (1994).
- [18] C. V. Somasundari, N. Neelakanda Pillai, C. K. Mahadevan, *Arch. Phy. Res.*, **3**,283 (2012).
- [19] R. Priya, G. Bhagavannarayana, S. Krishnan, S. Jerome Das, *Arch. Appl. Sci. Res.*, **2**,111 (2010).
- [20] K. Jaganathan S. Kalainathan, *J. Cryst. Growth*, **310**, 2043 (2008).
- [21] W. A. Wooster, *Rep. Progr. Phys.* **16**, 62 (1953).
- [22] Jain John, P. Christuraj, K. Anitha, T. Balasubramanian, *Mater. Chem. Phys.*, **118**, 284 (2009).

*Corresponding author: kalainathan@yahoo.com